Noise-Resilient SDR-Based Hybrid Deep Learning Framework for Robust Contactless Respiratory Monitoring

Rehan Khan, Umer Saeed, and Insoo Koo

***Abstract*—Respiratory patterns reflect critical physiological parameters such as rate, rhythm and depth that are closely associated with an individual's health status and potential respiratory disorders. Continuous, contactless monitoring enables early identification of abnormal respiratory behaviors, supporting preventive and remote healthcare. This study presents a contactless respiratory monitoring framework integrating software-defined radio (SDR) sensing with a hybrid deep learning model for accurate respiratory pattern recognition. The proposed architecture combines convolutional neural networks (CNNs), bidirectional long short-term memory (BiLSTM) networks and an attention mechanism to learn spatiotemporal dependencies from channel state information signals. A dual-USRP SDR platform was used to collect data from five healthy volunteers reproducing eight respiratory patterns under controlled behavioural simulation and a fixed transceiver geometry. To emulate representative deployment-related disturbances, a time-varying, non-stationary synthetic noise framework comprising additive white Gaussian noise (AWGN), baseline drift, narrowband interference, transient disturbances and signal-coupled artifacts was applied to the laboratory-controlled dataset. Experimental evaluation yielded mean accuracies of 99.97 ± 0.04% and 99.94 ± 0.11% for the laboratory-controlled and noise-injected datasets, respectively. Direct benchmarking against CNN–Transformer, Diffusion + CNN–Transformer and TSLANet under the same evaluation protocol further demonstrated that the proposed model achieved the highest classification accuracy while maintaining favorable computational efficiency. These findings provide a proof-of-concept for respiratory sensing under controlled behavioural conditions and demonstrate its potential for future validation in clinical and home-care environments and on embedded devices.**

***Index Terms*—software-defined radio, respiratory monitoring, deep learning, channel state information, attention mechanism.**

I. Introduction

RECENT advancements in the Internet of Things (IoT) have significantly transformed digital healthcare, enabling the continuous monitoring, recording and analysis of vital physiological signals to enhance the quality of life and enable the early detection of various health disorders [1]. Among these physiological indicators, respiration plays a critical role as it supports fundamental physiological processes and is closely associated with both physical and psychological health. A single respiratory cycle, consisting of inspiration and expiration, not only regulates gas exchange but also provides valuable clinical insights. Abnormal respiratory patterns have been widely recognized as early warning signs of life-threatening medical conditions, such as cardiac arrest, and may require intensive care intervention [2].

Several studies have shown that respiratory parameters serve as more reliable and sensitive indicators than other vital signs, such as heart rate or blood pressure, for distinguishing healthy individuals from those with underlying medical conditions [3]. Despite this, respiratory health remains considerably underappreciated, even though the World Health Organization identifies respiratory diseases as major global contributors to morbidity and mortality [4]. Viral infections, including influenza and COVID-19, further intensify this global respiratory health burden. Accurate and timely diagnosis is particularly critical, as respiratory illnesses often exhibit overlapping clinical symptoms, thereby increasing the risk of misdiagnoses [5]. Such diagnostic delays not only elevate morbidity and mortality rates but also facilitate the rapid spread of infectious diseases, emphasizing the need for robust, precise diagnostic techniques to support early diagnosis and appropriate intervention.

Respiratory patterns are critical indicators of physiological health, with deviations reflecting cardiopulmonary, neurological, metabolic and sleep-related disorders [6]. Clinically significant abnormalities include bradypnea, tachypnea, sighing respiration, Biot's respiration, Cheyne–Stokes respiration, Kussmaul respiration and Central Sleep Apnea (CSA). Prior contactless monitoring studies emphasize variations in respiratory rate, rhythm and depth as primary diagnostic indicators. These patterns range from early warning signs such as bradypnea and tachypnea [7], [8] to severe manifestations associated with neurological, cardiovascular or metabolic disorders (Table. I), including Cheyne–Stokes respiration, Kussmaul respiration and CSA [8], [9]. However, outside clinical environments such abnormalities are often underrecognized due to reliance on contact-based assessments, which restrict continuous monitoring and timely intervention. Additionally, many other abnormal patterns are rare or diagnostically overlapping, introducing ambiguity and class imbalance in data-driven models [7].

Current respiratory monitoring techniques are generally categorized into contact-based and contactless approaches. Contact-based systems, though highly accurate and considered the clinical gold standard for short-term assessments, provide precise diagnostic and therapeutic insights [10]. However, they are often intrusive and uncomfortable, requiring multiple electrodes that increase infection risk and limit their practicality for prolonged use [11]. In contrast, contactless modalities such as vision-based and radio-frequency (RF)-based sensing techniques enhance usability and user comfort by eliminating the need for physical contact. Recent studies demonstrate the practicality of contactless respiration monitoring using RF and

This research was supported by the Regional Innovation System and Education (RISE) program through the Ulsan RISE Center, funded by the Ministry of Education (MOE) and the Ulsan Metropolitan City Republic of Korea. (2026-RISE-07-001)

Rehan Khan and Insoo Koo are with the Department of Electrical Electronic and Computer Engineering, University of Ulsan, South Korea (e-mail: rehan77@mail.ulsan.ac.kr; iskoo@ulsan.ac.kr).

Umer Saeed is with the School of Computer Science and Technology, University of Bedfordshire, Luton, UK (e-mail: Umer.Saeed@beds.ac.uk).

TABLE I
CLINICALLY PRIORITIZED RESPIRATORY PATTERNS AND ASSOCIATED MONITORING RELEVANCE.

Respiratory Pattern	**Core Clinical Definition**	**Clinical Priority & Monitoring Relevance**
Eupnea	Normal, regular respiration (12–20 bpm)	Physiological baseline used for reference, calibration and comparative evaluation
Bradypnea	Abnormally slow respiration ($<$ 12 bpm)	Early-warning indicator of neurological or metabolic depression requiring timely monitoring
Tachypnea	Rapid, shallow respiration ($>$ 20 bpm)	Early indicator of cardiopulmonary stress, infection or metabolic imbalance
Biot's Respiration	Irregular respiration with unpredictable apnea	Critical marker of brainstem dysfunction and severe neurological abnormality
Cheyne–Stokes Respiration	Crescendo–decrescendo cycles with hypopnea	Severe cardiopulmonary and neurological disorder associated with high clinical risk
Kussmaul respiration	Deep, rapid, labored respiration	Medical emergency associated with metabolic acidosis requiring urgent intervention
Sighing Respiration	Intermittent deep breaths interrupting normal rhythm	Functional or stress-related respiratory dysregulation relevant to non-clinical monitoring
Central Sleep Apnea	Recurrent respiration pauses without respiratory effort	Chronic central respiratory control disorder requiring long-term monitoring

Wi-Fi sensing in consumer-oriented environments [12], [13]. Among these, radar-based sensing has emerged as particularly promising due to its non-intrusive operation, resilience to environmental interference and capability for continuous, real-time monitoring. Its significance became especially evident during the COVID-19 pandemic, when such systems significantly reduced infection risk while maintaining diagnostic reliability. Recent advancements in integrating radar within Integrated Sensing and Communication frameworks are now enabling next-generation intelligent healthcare applications.

Existing research on respiratory monitoring has primarily focused on establishing sensing feasibility and improving respiratory pattern classification using data collected under controlled laboratory environments. While these studies have achieved encouraging results, most evaluations have relied on relatively clean respiratory signals and emphasized classification accuracy as the primary performance measure. Consequently, the robustness of respiratory monitoring systems under practical deployment conditions, where environmental noise, hardware imperfections and electromagnetic interference are unavoidable, remains comparatively underexplored. To address this limitation, this study presents a wireless respiration monitoring framework that combines software-defined radio (SDR)-based sensing with a hybrid deep learning architecture integrating convolutional neural networks (CNNs), bidirectional long short-term memory (BiLSTM) networks and an attention mechanism.

In addition, a deployment-oriented noise model comprising time-varying additive white Gaussian noise (AWGN), non-stationary baseline drift, time-varying narrowband interference, transient disturbances and signal-coupled artifacts is intentionally applied to the clean respiratory signals. These perturbations vary over time and across recordings, providing a more representative assessment of model robustness under non-stationary sensing conditions. The proposed framework supports accurate recognition of eight respiratory patterns using both the laboratory-controlled data and the corresponding realistic noise-injected data. The main contributions of this work are summarized as follows.

(1) Development of an SDR-based contactless monitoring platform that enables unobtrusive monitoring of respiratory activity, facilitating the automatic recognition of distinct respiratory patterns.
(2) Design of a hybrid signal processing and deep learning framework that integrates a CNN–BiLSTM architecture with an attention mechanism to enhance recognition accuracy and ensure robust classification across eight distinct respiratory patterns.
(3) Implementation of a time-varying, non-stationary and partially signal-dependent noise-injection framework on laboratory-controlled data to emulate deployment-related disturbances and evaluate system robustness under diverse noise conditions.
(4) Comprehensive experimental validation using both laboratory-controlled and simulated noise-injected dataset, achieving high classification performance while demonstrating the reliability and robustness of the proposed framework.

The remainder of this paper is organized as follows. Section II provides a review of relevant literature on contactless respiratory monitoring techniques. Section III describes the proposed SDR–based platform and the hybrid deep learning architecture in detail. Section IV presents the experimental setup, performance results and corresponding analyses. Section V discusses the limitations of the present study and future research directions. Finally, Section VI concludes the paper by summarizing the key findings and discussing potential avenues for future research.

II. RELATED WORK

Contact-based and contactless approaches for respiration monitoring have been extensively explored in recent research. Contact-based techniques typically utilize wearable sensing devices such as smartwatches, thermocouples, thermistors and pyroelectric sensors to measure respiratory airflow and air temperature [14]. While these devices provide highly accurate

TABLE II
SUMMARY OF REPRESENTATIVE RF-BASED RESPIRATORY MONITORING STUDIES.

Ref.	Modality	Methodology	Respiratory Classes	Cost	Reported Performance	Main Contribution	Limitation
[18] (2017)	Wi-Fi CSI	TRRS + Root-MUSIC + SVM	1	Low	100%, 99%	Time- reversal framework for respiratory detection and multi-person respiratory rate estimation.	Limited to respiratory rate estimation only without respiratory pattern classification.
[19] (2018)	CW Radar	Feature Engineering + SVM	6	High	94.7%	CW-radar-based recognition of six respiratory disorders.	Limited to six respiratory classes and controlled sensing conditions.
[20] (2020)	Wi-Fi CSI	Doppler–AoA Mapping + DBSCAN	1	Low	98.8%, 98.4%, 97.5%	Multi-domain Doppler–AoA framework for respiration monitoring of three individuals using commodity Wi-Fi devices.	Limited to respiratory rate estimation and controlled indoor environments.
[21] (2021)	SDR RF	CSI Preprocessing + DMLP	6	Medium	99%	SDR-based identification of respiratory patterns using CSI amplitude and DMLP.	Limited to six respiratory classes and controlled laboratory experiments.
[22] (2021)	SDR RF	OFDM CSI Features + Complete Tree	6	Medium	99.4%	SDR-based classification of six respiratory patterns using OFDM CSI features.	Limited to six respiratory classes and controlled laboratory environments.
[23] (2021)	SDR RF	Curve-Fitting Augmentation + Machine learning	8	Medium	99.3%	Curve-fitting augmentation strategy for SDR-based classification of eight respiratory abnormalities.	Relied heavily on simulated data and controlled laboratory environments.
[17] (2021)	UWB Radar	Spectrogram + ResNet	2	High	90%	UWB radar classification of normal and tachypneic respiratory using spectrograms.	Limited to binary respiratory classification and controlled laboratory environments.
[6] (2022)	SDR RF	OFDM CSI Features + Ensemble Bagged Trees	3	Medium	99.7%, 93.3%, 88.4%	SDR-based respiratory classification framework extending from single- to multi-person scenarios.	Performance degrades with increasing subjects and relies on simulated illnesses in controlled environments.
[24] (2022)	SDR RF	CSI + Extra Trees	8	Medium	99%	Lightweight SDR framework for real and simulated CSI data for respiratory identification.	Relied heavily on simulated data and controlled laboratory environments.
[12] (2024)	Wi-Fi CSI	Dynamic GCN + GAF + E-GRU-D-MCNN	3	Low	96.67%	Wi-Fi-CSI framework for respiratory rate estimation and respiratory pattern recognition.	Limited to three healthy volunteers and controlled indoor environments.
[25] (2024)	Wi-Fi CSI	WCI + CNN-LSTM	6	Low	97.8%	Wi-Fi-based recognition of six respiratory patterns using CNN-LSTM.	Limited to six respiratory classes and controlled laboratory experiments.
[26] (2025)	Wi-Fi CSI	Diffusion-model Augmentation + GAF + CNN-Transformer	3	Low	98.3%	Diffusion-assisted Wi-Fi CSI framework for respiratory pattern recognition.	Limited to three respiratory classes and controlled laboratory evaluation.
[27] (2025)	CW Radar	ICA-JADE + MODWT	3	Medium	88.48%	Dual-subject respiratory pattern recognition across multiple postures using a CW radar.	Limited to three respiratory classes and controlled experiments with degraded performance in prone posture.
[28] (2025)	SDR RF	EMD-VMD + Kalman + CNN-BiLSTM	4	High	99.4%	Hybrid EMD–VMD SDR framework for classification of respiratory abnormalities.	Limited to four respiratory classes and controlled laboratory experiments.

and reliable measurements, they are often bulky, expensive and impractical for long-term continuous use, raising concerns regarding user comfort, hygiene and data privacy. These inherent limitations have led to increasing research interest in contactless sensing modalities, which offer unobtrusive, user-friendly and hygienic respiratory monitoring capabilities.

Recent advancements have increasingly emphasized RF-based contactless sensing for physiological and human activity monitoring, with AI-enabled approaches increasingly integrating radar, Wi-Fi and other RF modalities [15]. These approaches include radar systems, Wi-Fi–based sensing, optical camera–based imaging and SDR platforms [16]. By exploiting the propagation, reflection and scattering of electromagnetic waves from the human body, such systems can detect minute, respiration-induced chest wall displacements, enabling continuous and unobtrusive respiratory monitoring even during sleep [17]. The growing adoption of these technologies is primarily driven by their suitability for long-term deployment and the superior comfort and convenience they offer to users.

Camera-based respiration monitoring has been extensively explored as a visual, contactless approach using thermal and depth cameras to estimate respiratory rate from thoracic motion or nasal temperature variations [29]. Infrared thermography captures nostril temperature variations, while depth cameras detect minute chest wall displacements. Despite reasonable accuracy, these methods suffer from key limitations, including dependence on adequate illumination, restricted fields of view, inability to operate through obstructions, high computational demands and sensitivity to ambient temperature variations. Moreover, continuous video acquisition raises significant privacy concerns [30], limiting the suitability of camera-based systems for long-term, real-world or home-based respiratory monitoring applications.

Radar and Wi-Fi-based RF sensing have become widely investigated approaches for contactless respiratory monitoring. Radar modalities, including frequency modulated continuous wave (FMCW), ultra-wideband (UWB), and continuous-wave Doppler capture respiration through frequency shifts, time-of-flight measurements or periodic chest motion. Machine learning has further improved respiratory classification performance, while recent edge deep learning and transformer-based methods have highlighted the potential of RF sensing for practical healthcare applications [18], [31]–[33]. Wi-Fi-based approaches exploit Received Signal Strength (RSS) and Channel State Information (CSI) for low-cost, contactless respiratory monitoring [34]. Beyond respiratory sensing, recent studies have also demonstrated the effectiveness of deep-learning models on public Wi-Fi CSI datasets for contactless human activity recognition [35]. however, compared with SDR platforms, they are limited by restricted subcarrier availability, fixed operating bands and lower sensing flexibility [24], [36].

Recent CSI-based respiratory sensing studies have explored both amplitude and phase information. Several studies have demonstrated that calibrated or corrected CSI phase can provide useful respiratory information [37]–[39], while the complementary use of amplitude and phase has also been explored

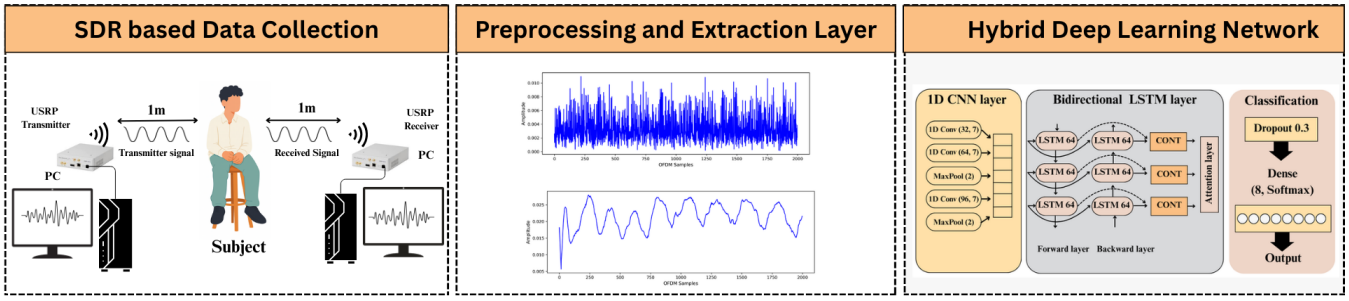

Fig. 1. Proposed SDR-based workflow for anomalous respiration identification, including RF data acquisition, signal preprocessing and hybrid CNN–BiLSTM–Attention-based classification.

[40]. Nevertheless, raw CSI phase is highly susceptible to synchronization errors and hardware impairments, typically requiring dedicated calibration or compensation before reliable physiological information can be obtained. By comparison, CSI amplitude is widely used for respiratory sensing because it offers a relatively stable signal representation, requires less complex preprocessing and has demonstrated reliable performance in practical sensing applications [40], [41].

SDR platforms address several limitations of conventional RF sensing systems by offering greater flexibility, reconfigurability and spectral resolution. A typical SDR setup employs two programmable radio units, one for transmission and one for reception, enabling dynamic control over bandwidth, subcarrier allocation and antenna configuration. Early studies demonstrated SDR-based respiration and heart-rate monitoring through obstacles using directional antennas and vector network analyzers [42], while subsequent work extended these capabilities to continuous-wave radar–based implementations [23]. More recently, CFR and CSI-derived features, combined with machine learning and deep learning models, have enabled multi-pattern respiratory classification, achieving recognition of up to eight abnormal respiratory categories [43], [44]. The Universal Software Radio Peripheral (USRP) further facilitates flexible single- and multi-subject experimentation, supporting the transition toward adaptive, contactless respiratory monitoring frameworks [21], [25].

Despite these advances, most RF, SDR, Wi-Fi and radar-based respiratory monitoring studies continue to emphasize improving respiratory pattern classification using signals collected under controlled laboratory conditions [21], [25], [43], [44]. Although these approaches have demonstrated promising results, their evaluations rely on relatively clean respiratory measurements and provide limited assessment of robustness under realistic deployment environments [21]. In addition, studies involving multiple monitored subjects consistently report performance degradation as the number of subjects increases because of increased signal complexity and inter-subject interference [20], [45], [46].

Moreover, many existing systems are limited to respiratory rate estimation or a relatively small number of respiratory classes [25], [44]. These limitations emphasize the need for more robust respiratory monitoring frameworks capable of maintaining reliable performance under practical operating conditions. To address this gap, this study proposes an SDR-based framework incorporating deployment-oriented noise modeling through time-varying AWGN, non-stationary baseline drift, time-varying narrowband interference, transient interference and signal-coupled disturbances, enabling rigorous robustness evaluation on laboratory-controlled and noise-injected datasets across eight respiratory patterns.

Table II summarizes representative RF-based contactless respiratory monitoring studies using Wi-Fi CSI, SDR, and radar sensing technologies. Earlier work mainly employed handcrafted signal-processing methods and conventional machine-learning algorithms, while recent studies have increasingly incorporated hybrid deep-learning architectures, Transformer-based models, and diffusion-assisted data augmentation [12], [18], [19], [21], [22], [25], [26], [28]. However, these studies vary considerably in sensing modality, number of respiratory classes, subject configuration, task objective, dataset, and evaluation protocol. Accordingly, the reported performance values are included only to provide an overview of the existing literature and should not be interpreted as direct quantitative comparisons.

III. Methodology

The proposed framework presents an intelligent SDR-based contactless respiratory monitoring system capable of accurately classifying distinct respiratory patterns. By integrating a hybrid CNN–BiLSTM with an enhanced attention mechanism, the framework effectively captures spatial and temporal dependencies from CSI-derived respiratory signals for accurate and robust classification, as shown in Fig. 1. The framework utilizes laboratory-acquired respiratory data and enhances realism through synthetic noise injections to emulate real-world conditions and evaluate model resilience under deployment challenges.

A. System Model

The proposed methodology utilizes an SDR-based wireless sensing framework to monitor respiration by capturing fine-grained CSI variations in electromagnetic signals. Implemented on a desktop workstation running LabVIEW-integrated SDR software, the system employs two USRP NI-2922 units with omnidirectional antennas serving as the transmitter and receiver. In indoor environments, multipath propagation encodes both environmental reflections and respiration-induced

chest motion [47]. The captured CSI signals are preprocessed and analyzed to classify respiratory patterns. The overall architecture consists of three main modules: transmitter, wireless channel and receiver, as illustrated in Fig. 2.

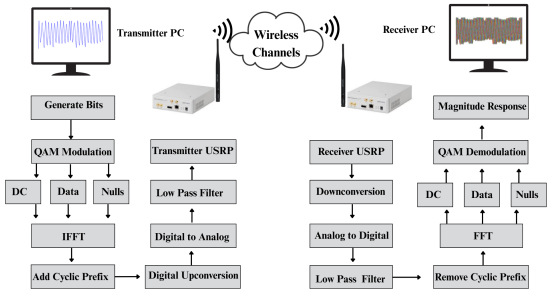

Fig. 2. Block diagram of the USRP-based wireless transceiver system used for respiratory signal acquisition.

1) Transmitter: The transmitter module comprises a host desktop computer connected to a USRP device. Random binary data are generated and modulated using quadrature amplitude modulation (QAM) to form parallel symbol streams. Reference symbols embedded in each frame enable precise channel estimation at the receiver. To reduce inter-symbol interference, a cyclic prefix (CP) is added by replicating the last quarter of the OFDM symbol and appending it; timing and frequency offsets are subsequently handled during receiver synchronization. Frequency-domain symbols are converted to the time domain via the inverse fast Fourier transform (IFFT). The resulting frames are transmitted at 20 MS/s baseband rate digitally up-converted to 400 MS/s for analog conversion and then filtered with a 20 MHz low-pass filter, frequency up-converted, amplified (0–30 dB) and radiated through an omnidirectional antenna.

2) Wireless Channel: The wireless channel captures minute signal variations induced by subtle thoracic and abdominal movements during respiration. These respiration-related displacements generate multipath propagation effects, which are quantified and represented using the CFR:

$$H(k) = \frac{Y(k)}{X(k)}, \tag{1}$$

where, $H(k)$ denotes the CFR, $X(k)$ represents the transmitted signal and $Y(k)$ corresponds to the received signal in the frequency domain. The CFR amplitude is computed as:

$$|H(k)| = \sqrt{H_{\text{Re}}^2 + H_{\text{Im}}^2}, \tag{2}$$

Where H_{Re} and H_{Im} denote the real and imaginary components, respectively. Although the estimated channel response provides both CSI amplitude and phase, this study specifically considers CSI amplitude to assess the robustness of amplitude-based respiratory pattern classification under realistic noise-injected sensing conditions. Calibrated CSI phase can also contain useful respiratory information; however, phase-based sensing generally requires dedicated calibration and compensation to reduce synchronization errors and hardware impairments before reliable physiological features can be extracted [37]–[41]. CSI amplitude was therefore adopted within the scope of this study because of its comparatively stable representation and established effectiveness in contactless respiratory monitoring. For each experiment, the CFR amplitude is continuously monitored across multiple OFDM frames, forming a matrix representation given by:

$$|H(k)|_E = \begin{bmatrix} |H(k)|_{1,1} & |H(k)|_{1,2} & \cdots & |H(k)|_{1,F} \\ |H(k)|_{2,1} & |H(k)|_{2,2} & \cdots & |H(k)|_{2,F} \\ \vdots & \vdots & \ddots & \vdots \\ |H(k)|_{I,1} & |H(k)|_{I,2} & \cdots & |H(k)|_{I,F} \end{bmatrix} \tag{3}$$

Here, I denotes the total number of OFDM subcarriers and F represents the total number of OFDM frames collected during a single experiment.

3) Receiver: At the receiver end, the USRP device captures the transmitted signal using an omnidirectional antenna. The received signal is initially amplified by a low-noise amplifier (LNA), followed by gain adjustment via a driver amplifier (DA) and subsequently down-converted through a Direct Conversion Receiver. The resulting baseband signal is then digitized by the ADC at 100 MS/s, filtered within a 20 MHz bandwidth and processed through a Digital Down Converter before being forwarded to the host system at 20 MS/s. At this stage, the CP is removed from each OFDM frame and frame synchronization is refined using the Van de Beek algorithm. Finally, a fast Fourier transform (FFT) converts the signal into the frequency domain, from which the CFR amplitude response is extracted for subsequent analysis and feature computation.

TABLE III
DEMOGRAPHIC DETAILS OF VOLUNTEERS PARTICIPATING IN DATA COLLECTION.

Sr. No.	Age (Years)	Gender	Weight (lb)	Height (in)	Body Mass Index	Physical Type
1	26	Male	167	68	25.4	Endomorph
2	28	Male	143	70	20.5	Ectomorph
3	31	Male	114	69	16.8	Endomorph
4	31	Male	143	68	21.7	Endomorph
5	31	Male	114	69	16.8	Ectomorph

B. Data Acquisition

The dataset analyzed in this study originates from our previously published works [21], [24], in which respiratory data were acquired under controlled laboratory conditions using a wireless SDR-based sensing platform comprising two USRP NI-2922 devices. Data collection involved five healthy adult volunteers with no reported respiratory, cardiovascular or neurological disorders, as summarized in Table III. Healthy participants were intentionally selected as the objective of this work was to establish a proof-of-concept evaluation of the proposed SDR-based respiratory sensing framework under controlled experimental conditions. Prior to data collection, all participants received detailed instructions and training to consistently reproduce the characteristic respiratory behaviours

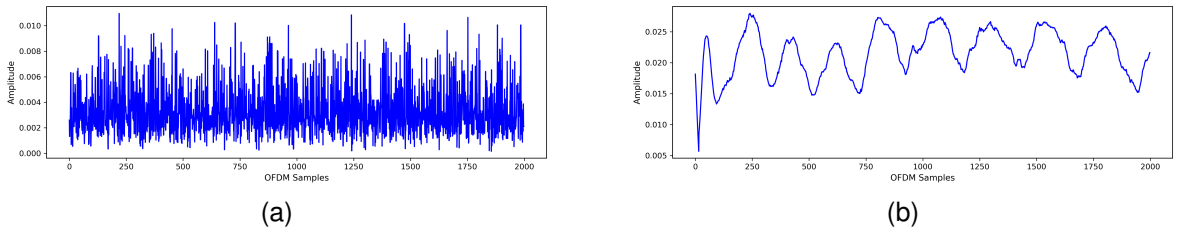

Fig. 3. Overview of the CSI amplitude preprocessing pipeline, (a) subcarrier selection and (b) normalization after noise suppression and smoothing.

associated with the target respiratory classes, thereby ensuring repeatable and reliable measurements throughout the experimental trials.

In the United Kingdom, research involving patients with medical disorders requires comprehensive ethical review, clinical governance approval and specialized recruitment procedures. Healthy volunteers were therefore considered suitable for this initial feasibility study, and the resulting recordings should be regarded as surrogate respiratory patterns reproduced under controlled behavioural simulation rather than clinically acquired pathological signals. Accordingly, this work represents a proof-of-concept sensing-feasibility investigation rather than a clinical diagnostic study. The transmitter and receiver were positioned one meter apart and aligned parallel to the participant's abdominal region, while participants maintained a relaxed posture with minimal movement under medical supervision.

The transmitter and receiver separation, participant posture and sensing geometry were intentionally maintained constant throughout the data acquisition campaign to ensure repeatable measurements and a consistent baseline for respiratory-pattern recognition. Each participant completed repeated trials covering eight respiratory patterns: eupnea, bradypnea, tachypnea, sighing respiration, Biot's respiration, Cheyne–Stokes respiration, Kussmaul respiration and CSA. Each trial lasted 30 s, resulting in 150 labeled experiments for signal-level analysis. Variations in body orientation, propagation conditions, sensing distance and simultaneous multi-subject monitoring were not examined during the data acquisition campaign.

C. Preprocessing Layer

The acquired SDR-based CSI recordings were subjected to a comprehensive preprocessing and quality-assurance pipeline before feature extraction. First, unstable acquisitions, corrupted packets and abnormal signal recordings were removed through quality-control procedures. The remaining CSI measurements were then processed to enhance respiration-induced channel variations while suppressing irrelevant noise. Although both CSI amplitude and phase can be derived from the estimated channel response, the preprocessing pipeline was finalized using CSI amplitude, and only the standardized amplitude signals were retained in the final dataset for subsequent analysis and model development. Consequently, raw synchronized CSI phase data were not preserved at the final preprocessing stage, precluding retrospective phase-only or amplitude–phase fusion analysis using the available dataset. The following preprocessing stages therefore operate exclusively on CSI amplitude signals and consist of four sequential processing steps.

1) Subcarrier Selection and Filtering: The first preprocessing stage involved identifying subcarriers with high sensitivity to respiratory activity. Although the receiver captured 256 OFDM subcarriers, those with minimal variance and thus weak sensitivity were discarded. Specifically, the variance of each subcarrier was computed and any subcarrier with a variance value below 0.0001 was removed from further analysis. The threshold value of 0.0001 was adopted based on variance-based subcarrier selection approaches reported in previous literature and empirically verified on our dataset, where it effectively removed low-variance, respiration-insensitive subcarriers while preserving informative respiration-related subcarriers. This procedure effectively eliminated low-sensitivity subcarriers while retaining those that demonstrated strong respiration-related signatures (Fig. 3(a)). The variance was calculated using Equation (4), where x_i represents the ith sample, $\bar{x}_k$ denotes the mean of the kth subcarrier and n indicates the total number of samples.

$$\text{var}_k = \frac{1}{n-1} \sum_{i=0}^{n-1} (x_i - \bar{x}_k)^2 \tag{4}$$

2) Outlier Detection and Removal: Following subcarrier selection, wavelet-based filtering was applied to suppress outliers while preserving critical signal transitions associated with respiratory activity. A soft-thresholding heuristic was employed, utilizing scaled noise parameters at the level-4 detail coefficients within the Symlets-5 (sym5) wavelet family. This approach provided effective signal smoothing while maintaining the structural integrity of respiration-induced variations, thereby ensuring that essential temporal features remained unaltered for subsequent analysis.

3) Signal Smoothing and Noise Suppression: To further attenuate high-frequency noise components unrelated to respiratory motion, a moving average filter with a window size of eight samples was applied. This step enhanced the clarity and smoothness of the respiratory signals, making distinct respiratory patterns more distinguishable and consistent across observations. The moving average filter of size $M = 8$ was implemented as defined in Equation (5), where $y[n]$ represents the filtered output, $x[n]$ denotes the input signal and M corresponds to the filter window length.

$$y[n] = \frac{1}{M} \sum_{k=0}^{M-1} x[n-k] \tag{5}$$

4) Feature Scaling and Normalization:: In the final preprocessing stage, normalization was applied to scale the respiratory signals within a fixed range of $[-1, 1]$. This standardization step ensured uniformity across datasets and facilitated stable convergence during the training of the deep learning model. Equation (6) was employed to shift and rescale the raw waveform, producing the normalized signal for each subcarrier, as illustrated in Fig. 3(b).

$$\overline{y}[n] = \frac{y[n] - offset}{scale}, \tag{6}$$

where $y[n]$ denotes the input data and $\overline{y}[n]$ represents the normalized output. The normalized waveform is obtained by shifting and scaling the input waveform according to the defined transformation.

D. Real-World Noise Modeling and Injection

Contactless RF-based systems, including USRP platforms, enable unobtrusive and continuous respiratory monitoring. In this study, CSI amplitude traces were collected under controlled laboratory conditions, producing clean and interpretable respiratory signals. However, practical deployment in environments such as hospital wards and home-care settings introduces environmental noise, hardware imperfections and unintended disturbances that can distort respiratory waveforms and reduce model robustness. Unlike our earlier study [48], which employed artificial fault injection, and prior work that mainly focused on noise suppression using filtering or adaptive techniques [49], the present work deliberately introduces realistic noise into clean respiratory signals to emulate deployment-related conditions and evaluate model robustness under both laboratory-controlled and noise-injected scenarios.

Respiratory data were acquired under highly controlled environments using a fixed transmitter–receiver geometry, relaxed participant posture and minimal body movement. Under these static conditions, representative impairments include hardware noise, slow baseline variations and electromagnetic interference. To better emulate practical sensing environments, the proposed noise model incorporates temporal variability, non-stationarity, transient interference and signal-dependent perturbations. AWGN, baseline drift and narrowband interference vary over time within each respiratory sequence, while transient burst interference and signal-coupled disturbances represent intermittent and waveform-dependent impairments. The key parameters of the time-varying and non-stationary noise model are summarized in Table IV. Let $s[n]$ denote a laboratory-controlled respiratory waveform of length N; the corresponding noise-injected observation is defined as

$$y[n] = s[n] + n_{\mathrm{AWGN}}[n] + d[n] + h[n] + b[n] + c[n], \tag{7}$$

where $n_{\mathrm{AWGN}}[n]$ represents time-varying AWGN, $d[n]$ denotes non-stationary baseline drift, $h[n]$ represents time-varying narrowband interference, $b[n]$ denotes transient burst interference and $c[n]$ represents the signal-coupled disturbance.

TABLE IV
KEY PARAMETERS OF THE TIME-VARYING AND NON-STATIONARY NOISE MODEL.

Component	Value / Setting
Record length	$N = 3500$ samples
Time-varying Gaussian noise	SNR: 18–26 dB
Non-stationary baseline drift	$A_d = 2.5 \times 10^{-4}$; 1.5 cycles/record; $\pm 30\%$ variation
Time-varying narrowband interference	$A_h = 1.0 \times 10^{-4}$; 50/60 cycles/record; $\pm 1\%$ variation
Transient interference	1–3 events/sequence; duration 1–4%
Signal-coupled disturbance	$\lambda \sim U(0.02, 0.08)$

***Additive White Gaussian Noise**:* AWGN is a random process with a zero-mean Gaussian distribution and flat spectral density across the frequency spectrum. In USRP receivers, it primarily arises from thermal agitation (Johnson–Nyquist noise) in resistive components, active circuit elements such as low-noise amplifiers (LNAs) and mixers, analog-to-digital converter (ADC) quantization errors and clock jitter [50]. This broadband noise is unavoidable.

$$P_s = \frac{1}{N} \sum_{n=0}^{N-1} s^2[n] \tag{8}$$

Instead of applying a single SNR value to the complete recording, the noise intensity is allowed to vary smoothly over time. Random SNR control points are selected within 18–26 dB and smoothly interpolated across the respiratory sequence. The instantaneous noise variance is therefore calculated as

$$\sigma^2[n] = \frac{P_s}{10^{\mathrm{SNR}[n]/10}}, \qquad \mathrm{SNR}[n] \in [18, 26] \text{ dB} \tag{9}$$

The corresponding time-varying Gaussian samples are generated as

$$n_{\mathrm{AWGN}}[n] \sim \mathcal{N}\left(0, \sigma^2[n]\right) \tag{10}$$

Thus, the Gaussian noise variance changes gradually throughout each recording rather than remaining constant across the complete respiratory sequence.

***Baseline Wander (Low-Frequency Drift)**:* Baseline wander is a low-frequency displacement of the signal baseline that can arise from slow sensor or environmental variations, posture-related effects or gradual changes in the measured respiratory waveform [51]. To produce a non-stationary baseline component, both drift amplitude and oscillation rate vary smoothly over time as

$$d[n] = A_d e_d[n] \sin\left(\frac{2\pi}{N} \sum_{i=0}^{n} f_d[i] + \phi_d\right), \qquad \phi_d \sim \mathcal{U}(0, 2\pi). \tag{11}$$

Here, $A_d = 2.5 \times 10^{-4}$ is the nominal drift amplitude, while $e_d[n]$ is a time-varying envelope ranging from 0.5 to 1.5. The nominal drift rate is 1.5 cycles per record, with $f_d[n]$ varying by approximately ±30% around this nominal value throughout the sequence.

Time-Varying Narrowband Interference: Narrowband interference can arise from periodic electronic or environmental disturbances and coupling into the RF signal chain [52]. Rather than remaining constant throughout the recording, both its amplitude and oscillation rate vary over time across the respiratory sequence:

$$h[n] = A_h e_h[n] \sin\left(\frac{2\pi}{N}\sum_{i=0}^{n} f_h[i] + \phi_h\right), \qquad \phi_h \sim \mathcal{U}(0, 2\pi). \tag{12}$$

Here, $A_h = 1.0 \times 10^{-4}$ denotes the nominal interference amplitude, while $e_h[n]$ is a time-varying envelope ranging from 0.4 to 1.6. A nominal interference rate of 50 or 60 cycles per record is randomly selected for each sequence, and $f_h[n]$ varies by $\pm 1\%$ around the selected nominal rate throughout the sequence.

Transient/Burst Interference: Real RF measurements may experience short-duration disturbances caused by intermittent electromagnetic activity, switching events or temporary environmental perturbations rather than continuous interference throughout a recording. To represent these non-stationary events, transient interference is introduced at randomly selected temporal locations within each respiratory sequence and modeled as

$$b[n] = \sum_{j=1}^{B} \alpha_j \sigma_s w_j[n] \epsilon_j[n] \tag{13}$$

where $B \in \{1, 2, 3\}$ denotes the number of transient events, σ_s is the standard deviation of the clean respiratory waveform, $\alpha_j \in [0.10, 0.30]$ controls the relative disturbance strength and $\epsilon_j[n] \sim \mathcal{N}(0, 1)$. The function $w_j[n]$ represents a Hann-window envelope applied over a randomly selected interval spanning approximately 1–4% of the complete signal length. The resulting disturbance is therefore confined to short temporal segments and is inherently non-stationary.

Signal-Coupled Disturbance: Beyond independent additive disturbances, practical sensing conditions may introduce perturbations whose magnitude depends on the underlying respiratory waveform. To emulate this behavior, a synthetic signal-coupled component is defined as

$$c[n] = \lambda\big(s[n] - \bar{s}\big) e_c[n] \tag{14}$$

where $\bar{s}$ denotes the mean amplitude of the clean respiratory sequence, $\lambda \sim \mathcal{U}(0.02, 0.08)$ is the coupling coefficient and $e_c[n]$ is a time-varying random envelope within $[-1, 1]$. Because this perturbation scales directly with the centered respiratory waveform, its magnitude varies with the underlying signal rather than behaving as an entirely independent additive disturbance.

E. Proposed Attention-Enhanced CNN–BiLSTM Framework

Following preprocessing, each respiratory signal was represented as a sequence of 3,500 data samples, with each sequence labeled according to its corresponding respiratory pattern. To establish a performance benchmark, three baseline architectures: a CNN, a BiLSTM network and a hybrid CNN–BiLSTM model were evaluated and compared against the proposed attention-enhanced CNN–BiLSTM framework. The proposed attention-enhanced CNN–BiLSTM architecture was subsequently trained on the preprocessed datasets following a sequential end-to-end pipeline as outlined below.

1) Convolutional Feature Extraction (1D-CNN): The CNN module is designed to extract hierarchical local features from preprocessed CSI-derived respiratory signals, capturing patterns from low-level waveforms to high-level representations. A sequence of Conv1D layers with progressively increasing filters is employed to model complex temporal structures within the input sequences. Each convolutional layer applies kernels (filters) to input feature maps, enabling the extraction of discriminative features such as signal morphology, local variations and short-term dependencies. Max-pooling layers follow selected convolutional layers to reduce feature dimensionality while preserving the most salient information.

The convolution operation for the ith feature map in the kth layer is mathematically expressed as:

$$y_i^{(k)} = \mathrm{ReLU}\left(\sum_{l=1}^{c^{(k-1)}} z_l^{(k-1)} * w_l^{(k)} + b_i^{(k)}\right), \tag{15}$$

where $z_l^{(k-1)}$ denotes the lth input feature map from the previous layer, $w_l^{(k)}$ is the convolution kernel and $b_i^{(k)}$ is the bias term. The rectified linear activation is defined as:

$$\mathrm{ReLU}(p) = \max(0, p) \tag{16}$$

In the lightweight architecture, three convolutional layers with 24, 32, and 48 filters are employed using kernel sizes of 7, 5, and 5, respectively. Max-pooling operations follow the first two convolutional layers to progressively reduce temporal dimensionality while retaining salient respiration-related features. A dropout rate of 0.30 is applied after the final convolutional block for regularization. The resulting feature maps are then passed to a BiLSTM network for sequential pattern learning and temporal dependency modeling.

2) Temporal Modeling via BiLSTM: The BiLSTM network is an advanced variant of recurrent neural networks designed to model temporal dependencies within sequential data. Unlike standard LSTMs [53], BiLSTMs process input sequences in both forward and backward directions, enabling the model to capture contextual dependencies from both forward and backward time steps.

Each BiLSTM unit comprises three gating mechanisms the forget, input and output gates which collectively regulate information flow within the memory cell. The forward LSTM operations at time step t are defined as:

$$\begin{aligned} f_t &= \sigma(W_f[h_{t-1}, x_t] + b_f), \\ i_t &= \sigma(W_i[h_{t-1}, x_t] + b_i), \\ o_t &= \sigma(W_o[h_{t-1}, x_t] + b_o), \\ C_t &= f_t . C_{t-1} + i_t . \tanh(W_c[h_{t-1}, x_t] + b_c), \\ h_t &= o_t . \tanh(C_t), \end{aligned} \tag{17}$$

where x_t denotes the input vector at time step t, h_{t-1} and C_{t-1} represent the previous hidden and cell states, respectively and $\sigma(\cdot)$ is the sigmoid activation function.

The backward LSTM processes the sequence in reverse order (from the last time step to the first) using analogous equations but with a distinct set of weight matrices W'_f, W'_i, W'_o, W'_C and bias vectors b'_f, b'_i, b'_o, b'_C. The forward and backward hidden states at time step t are then concatenated to form the final hidden representation:

$$h_t = [h_t, h'_t], \tag{18}$$

Where h_t and h'_t denote the forward and backward hidden states, respectively. This bidirectional mechanism enables the network to leverage contextual information from both preceding and succeeding time steps, resulting in a comprehensive temporal understanding of respiratory dynamics. Consequently, the BiLSTM network enhances representational capacity, robustness and classification accuracy in respiratory pattern recognition tasks. In the proposed lightweight configuration, the BiLSTM layer employs 32 units in each direction, resulting in a 64-dimensional bidirectional representation. A dropout rate of 0.40 is applied within the BiLSTM layer to improve regularization while maintaining a compact temporal representation.

3) Attention-Based Feature Refinement: The integration of CNN and BiLSTM networks provides a robust foundation for respiratory pattern classification. While the BiLSTM effectively captures sequential dependencies, not all time steps contribute equally to the final classification outcome. Therefore, an attention mechanism is incorporated to identify and emphasize the most informative temporal regions of the respiratory sequence. For each BiLSTM output h_t, an intermediate attention score μ_t is computed and normalized using a softmax function as follows:

$$\alpha_t = \frac{\exp(\mu_t)}{\sum_{j=1}^{T} \exp(\mu_j)} \tag{19}$$

Here T denotes the total number of time steps and α_t represents the normalized attention weight corresponding to time step t. The final context vector v is then obtained as a weighted sum of all BiLSTM hidden outputs, defined as:

$$v = \sum_t \alpha_t h_t \tag{20}$$

This attention mechanism enables the model to adaptively emphasize critical respiratory cycles and temporal variations most relevant for classification, thereby enhancing both accuracy and interpretability.

4) Final Classification Layer: The context vector v from the attention layer is passed to a fully connected softmax layer with eight output neurons to generate class probability distributions. The proposed lightweight model was trained using the Adam optimizer with a learning rate of 1×10^{-3}, a batch size of 64, and sparse categorical cross-entropy loss for up to 50 epochs, with early stopping and learning-rate reduction applied to prevent overfitting.

TABLE V
HARDWARE AND SOFTWARE CONFIGURATION PARAMETER SETTINGS.

Hardware configuration parameters	
SDR device	NI USRP-2922 (Dual USRP: Tx & Rx)
Antenna type	Omnidirectional
Bandwidth	20 MHz
Baseband sampling rate	20 MS/s
ADC sampling rate	100 MS/s
DAC rate	400 MS/s
Transmitter gain	0–30 dB (software controlled)
Receiver gain	LNA + Driver Amplifier
Tx–Rx distance	1 m
Software configuration parameters	
Modulation scheme	QAM
Bits per symbol	2
OFDM subcarriers	256
Signal representation	CSI amplitude time series
Data acquisition duration	30 s per trial

IV. EXPERIMENTS AND RESULTS

This section provides a comprehensive evaluation of the proposed attention-enhanced CNN–BiLSTM framework for respiratory pattern classification. The analysis covers multiple performance metrics and controlled comparisons with conventional baseline models and recent advanced deep learning architectures. It first describes the experimental setup and dataset characteristics, followed by a detailed assessment of classification performance across different model configurations, and concludes with an evaluation of computational efficiency. Both laboratory-acquired and time-varying, non-stationary noise-injected datasets were used to assess robustness, while CNN–Transformer, Diffusion + CNN–Transformer and TSLANet were directly benchmarked using the same experimental protocol.

A. Experimental Setup

A series of controlled experiments was conducted to evaluate the proposed deep learning architecture. All model-training and evaluation experiments were executed on a high-performance workstation equipped with an AMD Ryzen 9 5900X 12-core CPU, 64 GB RAM and an NVIDIA GeForce RTX 3080 GPU with 10 GB GDDR6X memory. Model development and evaluation were carried out in Python 3.9.18 using TensorFlow 2.10.1 with the Keras API, supported by CUDA and cuDNN. NumPy, Matplotlib and Scikit-learn were used for data processing, visualization and metric computation. This configuration provided a stable, high-throughput platform for model training and validation. All reported prediction speed, inference latency and training time therefore correspond to workstation-based execution. Accordingly, the present implementation should be regarded as a feasibility evaluation of the proposed SDR-based respiratory pattern recognition framework rather than a direct assessment of embedded or edge-device deployment.

Respiratory data were acquired in a controlled, office-sized laboratory environment to ensure repeatability and minimize uncontrolled disturbances affecting CSI measurements. The Tx–Rx distance, participant posture and sensing geometry were kept fixed because the study focuses on robustness to

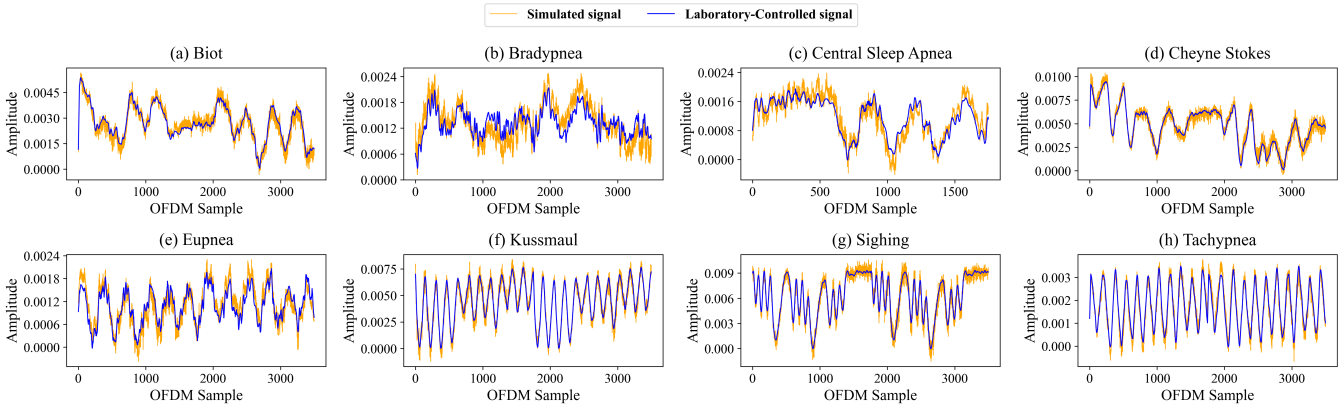

Fig. 4. Laboratory-controlled and non-stationary noise-injected respiratory waveforms for eight respiratory patterns, illustrating the effects of time-varying, transient, and signal-dependent disturbances on respiratory signal morphology: (a) Biot, (b) Bradypnea, (c) CSA, (d) Cheyne–Stokes, (e) Eupnea, (f) Kussmaul, (g) Sighing, and (h) Tachypnea.

signal-level noise rather than variability in physical operating conditions. The room contained only stationary objects, including walls, desks, chairs, computers and measurement equipment, with no additional human activity during acquisition. CSI signals were captured using USRP transceivers with omnidirectional antennas, where multipath propagation and body reflections encoded respiration-induced chest and abdominal motion into the channel response. Indoor temperature and relative humidity were maintained within stable ranges to limit unintended RF front-end drift or attenuation. This controlled baseline enabled systematic evaluation of AWGN, baseline drift, narrowband interference, transient disturbances and signal-coupled perturbations.

Five volunteers contributed data covering eight respiratory patterns, with each 30 s trial producing approximately 3,650 OFDM symbols and yielding datasets of 8×3,650×3,500 samples; the corresponding hardware and software configurations are summarized in Table V. Two dataset versions were evaluated: a clean laboratory-controlled set and a non-stationary noise-injected simulated set generated using the revised time-varying and signal-dependent disturbance framework to assess robustness under more challenging deployment-oriented conditions. Separate experimental pipelines were used for the clean and noisy datasets, with models trained and tested independently.

In each pipeline, the data were partitioned into training 70%, validation 15% and testing 15% sets, with splitting performed independently to ensure that clean laboratory-controlled and simulated noise-injected samples were never mixed and that no identical or correlated samples appeared across training and testing sets, thereby preventing information leakage and ensuring unbiased performance evaluation. To evaluate statistical robustness and reduce the influence of random weight initialization and training stochasticity, each deep learning model was independently trained and evaluated over five runs using different random seeds while maintaining the same experimental protocol. The final classification metrics are reported as the mean ± standard deviation across the five runs.

TABLE VI
FINAL CNN–BILSTM TRAINING PARAMETERS.

Parameter	Search Range Explored	Final Value
Learning rate	$\{1\times10^{-4}, 5\times10^{-4}, 1\times10^{-3}\}$	1×10^{-3}
Batch size	{32, 64, 128}	64
Epochs (max)	50	50
Dropout rate	[0.30 – 0.50]	0.30, 0.40
BiLSTM units	{32, 48, 64}	32
Attention dimension	–	24

B. Respiratory Data

This subsection describes the respiratory patterns analyzed using SDR-based RF sensing, with CSI amplitude serving as the primary feature for evaluation. Respiratory data were collected from healthy volunteers trained to consistently reproduce the characteristic breathing behaviours associated with the target respiratory classes under controlled laboratory conditions. Fig. 4 shows the eight representative respiratory patterns recorded during the experiments together with the corresponding signals generated using the revised non-stationary noise framework. The simulated traces incorporate time-varying Gaussian noise, non-stationary drift, time-varying narrowband interference, transient disturbances and signal-coupled perturbations while preserving the underlying respiratory morphology. The recorded patterns should therefore be interpreted as surrogate respiratory behaviours for evaluating the proposed SDR sensing framework rather than as clinically validated pathological respiratory events.

a) Biot: Biot's respiration is characterized by clusters of deep, irregular breaths followed by intervals of apnea. As shown in Fig. 4(a), the respiratory pattern exhibits erratic amplitude fluctuations interspersed with brief cessations of airflow and irregular deep inhalations.

b) Bradypnea: Bradypnea refers to abnormally slow and shallow respiration with a consistent rhythm. As depicted in Fig. 4(b), approximately six breaths are observed within 30 seconds, reflecting a clinically sluggish respiratory rate.

c) Central Sleep Apnea: CSA is marked by repetitive pauses in respiration during sleep, followed by the resumption of normal respiratory activity. As shown in Fig. 4(c), the

TABLE VII
PERFORMANCE COMPARISON OF DEEP LEARNING MODELS ON LABORATORY-CONTROLLED AND SIMULATED RESPIRATORY DATASET (MEAN ± STANDARD DEVIATION OVER 5 RUNS).

Model	Laboratory-Controlled Dataset				Simulated Dataset			
	Accuracy (%)	Precision (%)	Recall (%)	F1-score (%)	Accuracy (%)	Precision (%)	Recall (%)	F1-score (%)
CNN	92.12 ± 0.60	92.32 ± 0.74	92.12 ± 0.60	92.08 ± 0.67	80.11 ± 9.44	80.81 ± 8.21	80.10 ± 9.44	79.91 ± 9.52
BiLSTM	89.51 ± 15.43	90.17 ± 14.32	89.51 ± 15.43	89.33 ± 15.86	92.77 ± 12.13	93.11 ± 11.47	92.77 ± 12.13	92.72 ± 12.22
CNN + BiLSTM	98.79 ± 1.62	98.81 ± 1.61	98.79 ± 1.63	98.79 ± 1.63	95.68 ± 5.48	95.86 ± 5.15	95.68 ± 5.49	95.69 ± 5.46
CNN + BiLSTM + Attention	99.97 ± 0.04	99.97 ± 0.04	99.97 ± 0.04	99.97 ± 0.04	99.94 ± 0.11	99.94 ± 0.11	99.94 ± 0.11	99.94 ± 0.11

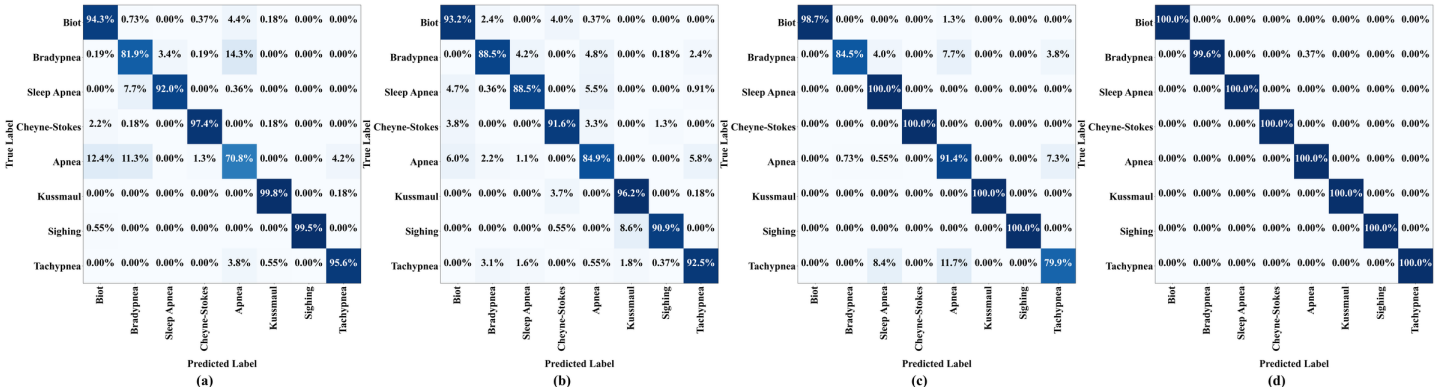

Fig. 5. Confusion matrices of the evaluated models for respiratory pattern classification. (a) CNN, (b) BiLSTM, (c) CNN–BiLSTM and (d) Attention-enhanced CNN–BiLSTM. The attention-based hybrid model achieves the most accurate and balanced classification across all respiratory classes.

waveform reveals intermittent cessations of airflow alternating with periods of regular respiratory motion.

d) Cheyne–Stokes: Cheyne–Stokes respiration exhibits a cyclic fluctuation in respiratory amplitude, characterized by gradual increases and decreases in tidal volume followed by apneic intervals. This oscillatory pattern is clearly depicted in Fig. 4(d).

e) Eupnea: Eupnea represents normal respiration, characterized by a steady and regular rhythm, typically ranging between 12 and 20 bpm. As shown in Fig. 4(e), approximately ten breaths occur within 30 seconds, which lies within the physiological range of normal respiration.

f) Kussmaul: Kussmaul's respiration is defined by deep, labored and rapid respiration, often associated with metabolic acidosis. As illustrated in Fig. 4 (f), the signal demonstrates a continuous and exaggerated pattern of inhalation and exhalation.

g) Sighing: Sighing respiration consists of normal respiratory cycles periodically interrupted by deep, exaggerated inspirations. Fig. 4(g) highlights this irregular pattern, where periodic sighs punctuate the regular respiratory rhythm.

h) Tachypnea: Tachypnea involves rapid and shallow respiration at a rate exceeding that of eupnea. As presented in Fig. 4(h), around 13 breaths occur within 30 seconds, indicating an accelerated respiratory rhythm.

C. Experimental Results

A multiclass classification framework was developed to distinguish eight respiratory activities. Four deep learning models, CNN, BiLSTM, CNN–BiLSTM and the proposed attention-enhanced CNN–BiLSTM, were trained and evaluated under identical training conditions. Hyperparameters were empirically tuned over predefined candidate ranges using a fixed stratified train–validation split. The search considered learning rates of $1 \times 10^{-4}, 5 \times 10^{-4}, 1 \times 10^{-3}$, batch sizes of $32, 64, 128$, dropout probabilities from 0.30 to 0.50, and BiLSTM units of $32, 48, 64$. The final lightweight model used convolutional filters of 24, 32 and 48, 32 BiLSTM units, an attention dimension of 24, a batch size of 64, and dropout rates of 0.30 and 0.40 for the CNN and BiLSTM stages, respectively. The selected training parameters are summarized in Table VI.

To provide a consistent basis for comparison, performance was evaluated using accuracy, precision, recall, F1-score, prediction speed, training time and confusion matrices. Prediction speed was expressed as the number of observations processed per second, whereas training time was measured in seconds. Together, these metrics enabled a detailed assessment of each model's ability to recognize respiratory patterns under diverse conditions.

Using this evaluation protocol, the four deep learning models were assessed on both laboratory-controlled and simulated datasets. Table VII reports the mean ± standard deviation over five independent runs for accuracy, precision, recall and F1-score. On the laboratory-controlled dataset, all models achieved strong performance. The proposed attention-enhanced CNN–BiLSTM obtained the highest results, with accuracy, precision, recall and F1-score all reaching $99.97 \pm 0.04\%$. Among the baseline models, CNN–BiLSTM achieved the highest average accuracy of $98.79 \pm 1.62\%$, followed by CNN at $92.12 \pm 0.60\%$ and BiLSTM at $89.51 \pm 15.43\%$. The CNN exhibited balanced precision and recall, whereas BiL-

TABLE VIII
COMPARISON OF MODEL COMPLEXITY, PREDICTION SPEED, INFERENCE LATENCY AND TRAINING TIME.

Model	Layers	Laboratory-Controlled Dataset			Simulated Dataset		
		Speed (obs/s)	Latency (ms/sample)	Train (s)	Speed (obs/s)	Latency (ms/sample)	Train (s)
CNN	7	36024	0.028	69	37635	0.027	68
BiLSTM	5	2318	0.434	846	2166	0.384	906
CNN-BiLSTM	6	3386	0.295	538	2517	0.397	569
CNN-BiLSTM+Attn.	9	8543	0.117	177	8803	0.114	193

STM showed greater variability across repeated runs. Incorporating the attention mechanism further improved classification performance and training consistency.

Under the simulated noise-injected conditions, performance varied across the baseline models. CNN achieved an average accuracy of $80.11 \pm 9.44\%$, while BiLSTM and CNN–BiLSTM reached $92.77 \pm 12.13\%$ and $95.68 \pm 5.48\%$, respectively. In contrast, the proposed lightweight attention-enhanced CNN–BiLSTM maintained consistently high performance, achieving average accuracy, precision, recall and F1-score of $99.94 \pm 0.11\%$ across five independent runs, indicating strong robustness and reproducibility under the revised noisy sensing conditions.

To further examine class-wise classification behavior, Fig. 5 presents the confusion matrices for the four evaluated models. For the CNN model (Fig. 5(a)), misclassifications mainly occurred between Eupnea and Biot's respiration and between Eupnea and Bradypnea, due to overlapping temporal and amplitude features. The BiLSTM model (Fig. 5(b)) exhibited higher confusion between Bradypnea and CSA as well as between Eupnea and CSA, reflecting limitations in temporal modeling when spatial feature extraction is absent. The CNN–BiLSTM hybrid (Fig. 5(c)) achieved nearly perfect performance (99.6% accuracy) by effectively combining spatial filtering and temporal feature learning. Finally, the attention-enhanced CNN–BiLSTM (Fig. 5(d)) achieved perfect classification, eliminating interclass confusion by focusing on salient temporal segments. Even complex patterns such as Cheyne–Stokes and Kussmaul's respiration were accurately identified, demonstrating strong class-wise discrimination.

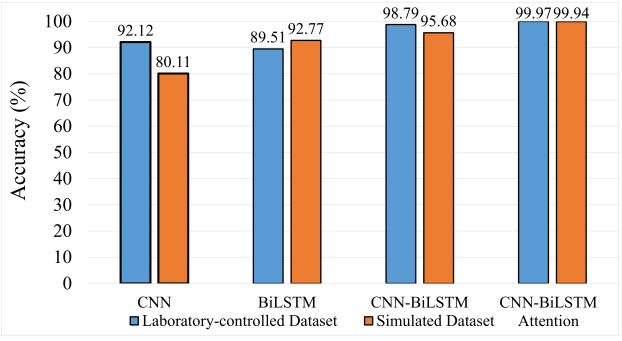

Fig. 6. Accuracy comparison of deep learning models on laboratory-controlled and simulated datasets.

Beyond classification performance, the models were compared in terms of architectural complexity, prediction throughput, inference latency and training time, as summarized in Table VIII. The CNN model (7 layers) achieved the highest inference speed of 36,024 obs/s, corresponding to 0.028 ms/sample latency and 69 s training time on the laboratory-controlled dataset. The BiLSTM model (5 layers) required 846 s of training and achieved 2,318 obs/s with 0.434 ms/sample latency. The lightweight CNN–BiLSTM model (6 layers) achieved 3,386 obs/s, 0.295 ms/sample latency and 538 s training time. The proposed lightweight attention-enhanced CNN–BiLSTM (9 layers) achieved 8,543 obs/s, 0.117 ms/sample latency and 177 s training time. On the simulated noise-injected dataset, the proposed model achieved 8,803 obs/s, 0.114 ms/sample latency and 193 s training time, demonstrating efficient computational performance on the workstation-based evaluation platform despite the enhanced noise conditions. Nevertheless, the current implementation represents a workstation-based feasibility validation rather than a deployment-ready embedded system.

TABLE IX
PERFORMANCE COMPARISON OF CONVENTIONAL SIGNAL-PROCESSING/MACHINE LEARNING METHODS AND DEEP LEARNING MODELS.

Model	Laboratory-Controlled Dataset	Simulated Dataset
	Accuracy (%)	Accuracy (%)
STFT + RF	96.19 ± 0.21	84.78 ± 0.31
Wavelet Packet + SVM	89.66 ± 0.36	68.37 ± 0.24
FFT Features + KNN	81.84 ± 0.60	86.08 ± 0.50
EMD + KNN	97.17 ± 0.19	75.41 ± 0.58
CNN	92.12 ± 0.60	80.11 ± 9.44
BiLSTM	89.51 ± 15.43	92.77 ± 12.13
CNN + BiLSTM	98.79 ± 1.62	95.68 ± 5.48
CNN-BiLSTM+Attn.	99.97 ± 0.04	99.94 ± 0.11

Fig. 6 presents a quantitative comparison of classification performance across the laboratory-controlled and simulated noise-injected datasets, illustrating the effect of realistic noise on respiratory pattern recognition. Although all evaluated models achieved competitive accuracy under clean conditions, performance generally declined after noise injection. The CNN showed the largest reduction, from 92.12% to 80.11%, indicating greater sensitivity to the introduced disturbances, while the BiLSTM retained competitive performance. The CNN–BiLSTM hybrid showed improved resilience, achieving approximately 98.79% accuracy on laboratory-controlled data and 95.68% under noisy conditions. In contrast, the proposed attention-enhanced CNN–BiLSTM maintained approximately 99.97% accuracy on the laboratory-controlled dataset and 99.94% on the simulated dataset, demonstrating consistently strong classification performance across both conditions.

Following the deep-learning analysis, representative conventional signal-processing and machine-learning approaches were evaluated using the same respiratory datasets. Four pipelines were considered: Short-Time Fourier Transform with Random Forest (STFT+RF), Wavelet Packet Transform with SVM (WPT+SVM), FFT with K-Nearest Neighbor (FFT+KNN) and Empirical Mode Decomposition with K-Nearest Neighbor (EMD+KNN). These approaches combine handcrafted feature extraction from time–frequency or signal-decomposition representations with conventional machine learning classifiers. Their performance, however, de-

TABLE X
DIRECT BENCHMARK COMPARISON OF RECENT ADVANCED DEEP LEARNING ARCHITECTURES UNDER THE SAME EVALUATION PROTOCOL.

Model	Layers	Laboratory-Controlled Dataset				Simulated Dataset			
		Accuracy (%)	Speed (obs/s)	Latency (ms/sample)	Train (s)	Accuracy (%)	Speed (obs/s)	Latency (ms/sample)	Train (s)
CNN-Transformer	32	99.28 ± 0.18	$4,195 \pm 94$	0.238 ± 0.005	519 ± 95	99.05 ± 0.25	$4,220 \pm 88$	0.237 ± 0.005	656 ± 106
Diffusion + CNN-Transformer	32	99.06 ± 0.24	$4,238 \pm 43$	0.236 ± 0.002	$2,553 \pm 91$	98.86 ± 0.31	$4,220 \pm 36$	0.237 ± 0.002	$2,887 \pm 196$
TSLANet	8	99.39 ± 0.15	$1,496 \pm 14$	0.669 ± 0.007	593 ± 1	99.18 ± 0.21	$1,484 \pm 33$	0.674 ± 0.015	807 ± 67
CNN-BiLSTM+Attn	**9**	$\mathbf{99.97 \pm 0.04}$	$\mathbf{8,543 \pm 234}$	$\mathbf{0.117 \pm 0.003}$	$\mathbf{177.2 \pm 27}$	$\mathbf{99.94 \pm 0.11}$	$\mathbf{8,803 \pm 148}$	$\mathbf{0.114 \pm 0.002}$	$\mathbf{193.2 \pm 45}$

TABLE XI
KEY CONFIGURATIONS OF THE EVALUATED DEEP LEARNING MODELS

Model	Key Configuration
CNN-BiLSTM+Attn.	Conv1D: 24→32→48; kernels: 7→5→5; BiLSTM: 32; attention: 24; batch: 64
CNN–Transformer	Conv1D: 64→128→128; kernels: 7→5→3; Transformer blocks: 2; embedding: 128; heads: 4; FFN: 256; batch: 16
Diffusion + CNN–Transformer	CNN–Transformer classifier + conditional 1-D DDPM; steps: 50; conditioning dim.: 64; dilations: {1,2,4,8}; synthetic augmentation: 20% per class; batch: 16
TSLANet	Patch: 8; stride: 4; embedding: 128; TSLA blocks: 2; MLP ratio: 3.0; batch: 16

pends strongly on manually engineered features, which may not sufficiently capture complex temporal dynamics and spectral variability, particularly under the revised noise conditions. To improve statistical robustness, each method was evaluated over five independent runs using different random seeds, with mean accuracy and standard deviation reported in Table IX. Although the conventional approaches achieved reasonable performance, the proposed deep learning architecture consistently obtained the highest classification accuracy on both the laboratory-controlled and simulated datasets.

Finally, to provide a fair benchmark against recent advanced deep-learning architectures, CNN–Transformer, Diffusion + CNN–Transformer and TSLANet [54] were directly implemented alongside the proposed model. Table XI summarizes the architecture-specific configurations, while all models were evaluated using identical datasets, preprocessing, data partitions, computational environment and repeated-run protocol. As reported in Table X, all advanced architectures achieved accuracies above 98.8% on both datasets. CNN–Transformer achieved 99.28 $\pm$ 0.18% and 99.05 $\pm$ 0.25% accuracy, while Diffusion + CNN–Transformer obtained 99.06 $\pm$ 0.24% and 98.86 $\pm$ 0.31% on the laboratory-controlled and simulated datasets, respectively.

TSLANet achieved $99.39 \pm 0.15\%$ and $99.18 \pm 0.21\%$, whereas the proposed attention-enhanced CNN–BiLSTM consistently achieved the highest accuracy of $99.97 \pm 0.04\%$ and $99.94 \pm 0.11\%$. The proposed model also provided higher prediction throughput (8,543 $\pm$ 234 and 8,803 $\pm$ 148 obs/s), lower inference latency (0.117 $\pm$ 0.003 and 0.114 $\pm$ 0.002 ms/sample), and shorter training times (177.2 $\pm$ 27 and 193.2 $\pm$ 45 s) than the compared advanced architectures. These results indicate that the proposed lightweight architecture achieves highly competitive predictive performance while offering a favorable balance between predictive performance and computational efficiency under both laboratory-controlled and simulated conditions.

V. LIMITATIONS AND FUTURE WORK

The proposed SDR-based respiratory monitoring framework achieved promising performance under laboratory-controlled and noise-injected conditions; however, several limitations remain. First, only standardized CSI amplitude responses were retained, while synchronized raw phase measurements were not preserved, preventing controlled comparisons among amplitude, phase, and fusion-based approaches. Future work will retain raw complex CSI and apply suitable phase calibration and correction. This proof-of-concept study also involved only five healthy volunteers under controlled behavioural simulation, with fixed Tx–Rx separation, standardized posture and single-subject monitoring. The findings therefore establish sensing feasibility rather than clinical diagnostic performance or robustness to variations in orientation, distance, propagation conditions, dynamic environments or multi-subject scenarios; future validation will include clinically diagnosed patients and broader physical configurations. Although the revised noise framework incorporates time-varying, non-stationary, transient and signal-coupled disturbances, these effects are synthetically generated, and future studies will incorporate recorded ambient interference and uncontrolled environments. Finally, despite reducing model complexity while maintaining low-latency performance, runtime evaluation remains workstation-based. Future work will investigate embedded and edge deployment, including memory utilization, power consumption and long-term operation.

VI. CONCLUSION

In this study, we presented a contactless SDR-based framework for robust respiratory pattern recognition. The proposed system combines signal processing with a hybrid deep learning architecture to accurately classify eight distinct respiratory patterns. Specifically, an attention-enhanced CNN–BiLSTM network was developed to capture spatiotemporal dependencies from CSI signals acquired using dual USRP transceivers. Experimental evaluation on laboratory-controlled and simulated non-stationary noise-injected datasets achieved accuracies of 99.97 ± 0.04% and 99.94 ± 0.11%, respectively. Direct benchmarking against CNN–Transformer, Diffusion + CNN–Transformer and TSLANet under the same evaluation protocol further showed that the proposed model achieved the highest accuracy among the evaluated models while maintaining favorable computational efficiency. The lightweight

architecture attained inference latencies of 0.117 and 0.114 ms/sample on the two datasets, respectively, while maintaining high throughput on the workstation platform. Moreover, incorporating time-varying AWGN, non-stationary baseline drift, time-varying narrowband interference, transient disturbances and signal-coupled artifacts enabled evaluation under more challenging deployment-oriented perturbations. Overall, the proposed SDR-based framework provides a robust proof-of-concept for accurate, computationally efficient and noise-resilient contactless respiratory pattern recognition, supporting future development and validation in clinical environments and on embedded devices for wireless respiratory monitoring.

REFERENCES

[1] J. Chen, S. Sun, L.-b. Zhang, B. Yang, and W. Wang, "Compressed sensing framework for heart sound acquisition in internet of medical things," *ieee transactions on industrial informatics*, vol. 18, no. 3, pp. 2000–2009, 2021.

[2] U. Saeed, S. Y. Shah, J. Ahmad, M. A. Imran, Q. H. Abbasi, and S. A. Shah, "Machine learning empowered covid-19 patient monitoring using non-contact sensing: An extensive review," *Journal of pharmaceutical analysis*, vol. 12, no. 2, pp. 193–204, 2022.

[3] D. Goldhill, A. McNarry, G. Mandersloot, and A. McGinley, "A physiologically-based early warning score for ward patients: the association between score and outcome," *Anaesthesia*, vol. 60, no. 6, pp. 547–553, 2005.

[4] S. M. Levine and D. D. Marciniuk, "Global impact of respiratory disease: what can we do, together, to make a difference?" *Chest*, vol. 161, no. 5, pp. 1153–1154, 2022.

[5] S. Sanduzzi Zamparelli, A. Sanduzzi Zamparelli, and M. Bocchino, "The evolving concept of the multidisciplinary approach in the diagnosis and management of interstitial lung diseases," *Diagnostics*, vol. 13, no. 14, p. 2437, 2023.

[6] M. Rehman, N. A. A. Ali, R. A. Shah, M. B. Khan, S. A. Shah, A. Alomainy, X. Yang, M. A. Imran, and Q. H. Abbasi, "Development of an intelligent real-time multiperson respiratory illnesses sensing system using sdr technology," *IEEE Sensors Journal*, vol. 22, no. 19, pp. 18 858–18 869, 2022.

[7] A. Al-Naji, K. Gibson, S.-H. Lee, and J. Chahl, "Monitoring of cardiorespiratory signal: Principles of remote measurements and review of methods," *Ieee Access*, vol. 5, pp. 15 776–15 790, 2017.

[8] M. Ali, A. Elsayed, A. Mendez, Y. Savaria, and M. Sawan, "Contact and remote breathing rate monitoring techniques: A review," *IEEE Sensors Journal*, vol. 21, no. 13, pp. 14 569–14 586, 2021.

[9] A. B. Obadi, P. J. Soh, O. Aldayel, M. H. Al-Doori, M. Mercuri, and D. Schreurs, "A survey on vital signs detection using radar techniques and processing with fpga implementation," *IEEE Circuits and Systems Magazine*, vol. 21, no. 1, pp. 41–74, 2021.

[10] Q. Wang, H. Cheng, and W. Wang, "Video-psg: An intelligent contactless monitoring system for sleep staging," *IEEE Transactions on Biomedical Engineering*, 2024.

[11] T. D. da Costa, M. d. F. F. Vara, C. S. Cristino, T. Z. Zanella, G. N. N. Neto, and P. Nohama, "Breathing monitoring and pattern recognition with wearable sensors," in *Wearable Devices-the Big Wave of Innovation*. IntechOpen, 2019.

[12] L. Zhang, R. Bao, C. Jiahao, and Y. Zhu, "Smart city healthcare: Non-contact human respiratory monitoring with wifi-csi," *IEEE Transactions on Consumer Electronics*, vol. 70, no. 3, pp. 5960–5968, 2024.

[13] M. F. Khan, G. Wang, Z. Zheng, and X. Liu, "Toward hybrid wi-fi halow radar csi coverage estimation in collapsed structures," *IEEE Transactions on Consumer Electronics*, vol. 70, no. 3, pp. 5201–5216, 2024.

[14] D. Liaqat, M. Abdalla, P. Abed-Esfahani, M. Gabel, T. Son, R. Wu, A. Gershon, F. Rudzicz, and E. D. Lara, "Wearbreathing: Real world respiratory rate monitoring using smartwatches," *Proceedings of the ACM on Interactive, Mobile, Wearable and Ubiquitous Technologies*, vol. 3, no. 2, pp. 1–22, 2019.

[15] T. Parveen, R. Khan, U. Saeed, and I. Koo, "Ai-enabled human activity recognition: Bridging contact-based and rf-based contactless sensing paradigms—a review," *IEEE Sensors Journal*, 2026.

[16] S. A. Shah, H. Abbas, M. A. Imran, and Q. H. Abbasi, "Rf sensing for healthcare applications," *Backscattering and RF Sensing for Future Wireless Communication*, pp. 157–177, 2021.

[17] U. Saeed, S. Y. Shah, A. A. Alotaibi, T. Althobaiti, N. Ramzan, Q. H. Abbasi, and S. A. Shah, "Portable uwb radar sensing system for transforming subtle chest movement into actionable micro-doppler signatures to extract respiratory rate exploiting resnet algorithm," *IEEE Sensors Journal*, vol. 21, no. 20, pp. 23 518–23 526, 2021.

[18] C. Chen, Y. Han, Y. Chen, H.-Q. Lai, F. Zhang, B. Wang, and K. R. Liu, "Tr-breath: Time-reversal breathing rate estimation and detection," *IEEE Transactions on Biomedical Engineering*, vol. 65, no. 3, pp. 489–501, 2017.

[19] H. Zhao, H. Hong, D. Miao, Y. Li, H. Zhang, Y. Zhang, C. Li, and X. Zhu, "A noncontact breathing disorder recognition system using 2.4-ghz digital-if doppler radar," *IEEE journal of biomedical and health informatics*, vol. 23, no. 1, pp. 208–217, 2018.

[20] Q. Gao, J. Tong, J. Wang, Z. Ran, and M. Pan, "Device-free multi-person respiration monitoring using wifi," *IEEE Transactions on Vehicular Technology*, vol. 69, no. 11, pp. 14 083–14 087, 2020.

[21] U. Saeed, S. Y. Shah, A. Zahid, J. Ahmad, M. A. Imran, Q. H. Abbasi, and S. A. Shah, "Wireless channel modelling for identifying six types of respiratory patterns with sdr sensing and deep multilayer perceptron," *IEEE Sensors Journal*, vol. 21, no. 18, pp. 20 833–20 840, 2021.

[22] M. Rehman, R. A. Shah, M. B. Khan, N. A. AbuAli, S. A. Shah, X. Yang, A. Alomainy, M. A. Imran, and Q. H. Abbasi, "Rf sensing based breathing patterns detection leveraging usrp devices," *Sensors*, vol. 21, no. 11, p. 3855, 2021.

[23] M. Rehman, R. A. Shah, M. B. Khan, S. A. Shah, N. A. AbuAli, X. Yang, A. Alomainy, M. A. Imran, and Q. H. Abbasi, "Improving machine learning classification accuracy for breathing abnormalities by enhancing dataset," *Sensors*, vol. 21, no. 20, p. 6750, 2021.

[24] U. Saeed, Q. H. Abbasi, and S. A. Shah, "Ai-driven lightweight real-time sdr sensing system for anomalous respiration identification using ensemble learning," *CCF Transactions on Pervasive Computing and Interaction*, vol. 4, no. 4, pp. 381–392, 2022.

[25] D. Fan, X. Yang, N. Zhao, L. Guan, M. M. Arslan, M. Ullah, M. A. Imran, and Q. H. Abbasi, "A contactless breathing pattern recognition system using deep learning and wifi signal," *IEEE Internet of Things Journal*, vol. 11, no. 13, pp. 23 820–23 834, 2024.

[26] X. Yang, T. Zhang, M. Zhou, B. Chen, Y. Wang, and R. Tong, "Csi-based respiratory pattern recognition using diffusion model and deep learning," *IEEE Transactions on Network Science and Engineering*, vol. 13, pp. 3894–3910, 2025.

[27] M. Shahriar, K. Ferdous, S. K. Pramanik, and S. M. Islam, "Non-contact monitoring and recognition of varied respiratory patterns from dual-subject across sleep postures using cw radar," *IEEE Journal of Electromagnetics, RF and Microwaves in Medicine and Biology*, 2025.

[28] M. M. Arslan, S. U. Rahman, A. A. Shah, N. Zhao, Z. Zhang, T. Cui, X. Yang, S. A. Shah, and Q. H. Abbasi, "Non-contact respiratory abnormality monitoring: A hybrid empirical mode and variational mode decomposition approach with software defined radio and deep learning," *IEEE Sensors Journal*, 2025.

[29] X. Mei and H. Ling, "Robust visual tracking and vehicle classification via sparse representation," *IEEE transactions on pattern analysis and machine intelligence*, vol. 33, no. 11, pp. 2259–2272, 2011.

[30] I. U. Din, A. Almogren, J. J. Rodrigues, and A. Altameem, "Advancing secure and privacy-preserved decision-making in iot-enabled consumer electronics via multimodal data fusion," *IEEE Transactions on Consumer Electronics*, 2024.

[31] K. Pervez, W. Aman, M. M. U. Rahman, M. W. Nawaz, and Q. H. Abbasi, "Hand-breathe: Noncontact monitoring of breathing abnormalities from hand palm," *IEEE Sensors Journal*, vol. 23, no. 20, pp. 25 136–25 143, 2023.

[32] C. Gianoglio, A. Rizik, E. Tavanti, D. D. Caviglia, and A. Randazzo, "On the edge recurrent neural network approach for ground moving fmcw radar target classification," *IEEE Transactions on Consumer Electronics*, vol. 70, no. 1, pp. 522–534, 2023.

[33] C. Fang, Y. Wang, M. Zhou, W. He, Q. Zhang, Y. Pang, and B. Peng, "End-to-end human motion recognition with multidomain dual attention transformer fusion network and millimeter-wave radar," *IEEE Transactions on Consumer Electronics*, 2025.

[34] H. Abdelnasser, K. A. Harras, and M. Youssef, "Ubibreathe: A ubiquitous non-invasive wifi-based breathing estimator," in *Proceedings of the 16th ACM international symposium on mobile ad hoc networking and computing*, 2015, pp. 277–286.

[35] T. Parveen, R. Khan, U. Saeed, and I. Koo, "Deep-learning-based baseline evaluation of public wifi csi datasets for contactless rf-based human activity recognition," *Sensors*, vol. 26, no. 12, p. 3821, 2026.

[36] S. A. Shah and F. Fioranelli, "Rf sensing technologies for assisted daily living in healthcare: A comprehensive review," *IEEE Aerospace and Electronic Systems Magazine*, vol. 34, no. 11, pp. 26–44, 2019.

[37] X. Wang, C. Yang, and S. Mao, "Phasebeat: Exploiting csi phase data for vital sign monitoring with commodity wifi devices," in *2017 IEEE 37th international conference on distributed computing systems (ICDCS)*. IEEE, 2017, pp. 1230–1239.

[38] Y. Zeng, D. Wu, J. Xiong, E. Yi, R. Gao, and D. Zhang, "Farsense: Pushing the range limit of wifi-based respiration sensing with csi ratio of two antennas," *Proceedings of the ACM on Interactive, Mobile, Wearable and Ubiquitous Technologies*, vol. 3, no. 3, pp. 1–26, 2019.

[39] X. Wang, C. Yang, and S. Mao, "Resilient respiration rate monitoring with realtime bimodal csi data," *IEEE Sensors Journal*, vol. 20, no. 17, pp. 10 187–10 198, 2020.

[40] Y. Zeng, D. Wu, R. Gao, T. Gu, and D. Zhang, "Fullbreathe: Full human respiration detection exploiting complementarity of csi phase and amplitude of wifi signals," *Proceedings of the ACM on Interactive, Mobile, Wearable and Ubiquitous Technologies*, vol. 2, no. 3, pp. 1–19, 2018.

[41] P. Kontou, S. B. Smida, and D. E. Anagnostou, "Contactless respiration monitoring using wi-fi and artificial neural network detection method," *IEEE Journal of Biomedical and Health Informatics*, vol. 28, no. 3, pp. 1297–1308, 2023.

[42] T. O. Praktika and A. Pramudita, "Implementation of multi-frequency continuous wave radar for respiration detection using software defined radio," in *2020 10th Electrical Power, Electronics, Communications, Controls and Informatics Seminar (EECCIS)*. IEEE, 2020, pp. 284–287.

[43] Y.-B. Tang and W.-C. Ge, "A novel ofdm symbol synchronization algorithm based on cyclic prefix in dvb-t," in *2008 4th International Conference on Wireless Communications, Networking and Mobile Computing*. IEEE, 2008, pp. 1–4.

[44] A. M. Ashleibta, Q. H. Abbasi, S. A. Shah, M. A. Khalid, N. A. AbuAli, and M. A. Imran, "Non-invasive rf sensing for detecting breathing abnormalities using software defined radios," *IEEE Sensors Journal*, vol. 21, no. 4, pp. 5111–5118, 2020.

[45] M. Rehman, R. A. Shah, N. A. A. Ali, M. B. Khan, S. A. Shah, A. Alomainy, M. Hayajneh, X. Yang, M. A. Imran, and Q. H. Abbasi, "Enhancing system performance through objective feature scoring of multiple persons' breathing using non-contact rf approach," *Sensors*, vol. 23, no. 3, p. 1251, 2023.

[46] D. Fan, T. Huang, L. Guan, J. Li, R. Fei, and L. Sevgi, "Noncontact multi-person respiration detection using time modulated array," *IEEE Sensors Journal*, 2025.

[47] Z. He, K. Deng, J. Gong, D. Wang, Z. Wang, and M. M. Salim, "Nuclear norm-based transfer learning for instantaneous multi-person indoor localization," *IEEE Transactions on Consumer Electronics*, 2024.

[48] R. Khan, U. Saeed, and I. Koo, "Robust sensor fault detection in wireless sensor networks using a hybrid conditional generative adversarial networks and convolutional autoencoder," *IEEE Sensors Journal*, 2025.

[49] N. S. Haider and A. K. Behera, "Respiratory sound denoising using sparsity-assisted signal smoothing algorithm," *Biocybernetics and Biomedical Engineering*, vol. 42, no. 2, pp. 481–493, 2022.

[50] D. Walter, A. Bülau, and A. Zimmermann, "Review on excess noise measurements of resistors," *Sensors*, vol. 23, no. 3, p. 1107, 2023.

[51] R. Gupta, "Biomedical sensors and data acquisition," in *Health Monitoring Systems*. CRC Press, 2019, pp. 19–56.

[52] S. Ha, C. Kim, Y. M. Chi, A. Akinin, C. Maier, A. Ueno, and G. Cauwenberghs, "Integrated circuits and electrode interfaces for noninvasive physiological monitoring," *IEEE Transactions on biomedical engineering*, vol. 61, no. 5, pp. 1522–1537, 2014.

[53] R. Khan, U. Saeed, and I. Koo, "Fedlstm: A federated learning framework for sensor fault detection in wireless sensor networks," *Electronics*, vol. 13, no. 24, p. 4907, 2024.

[54] E. Eldele, Z. Chen, M. Wu, X. Li, and M. Ragab, "Tslanet: Rethinking transformers for time series representation learning," in *AI for Time Series*. CRC Press, 2024, pp. 35–57.